Available online at www.sciencedirect.com
ScienceDirect
Pattern Recognition Letters 27 (2006) 1852–1862
Pattern Recognition Letters
www.elsevier.com/locate/patrec

Physical optics modelling of millimetre-wave personnel scanners

Beatriz Grafulla-González *, Katia Lebart, Andrew R. Harvey

Electrical, Electronic and Computing Engineering, School of Engineering and Physical Sciences, Heriot-Watt University, Edinburgh EH14 4AS, United Kingdom

Available online 17 April 2006

Abstract

We describe the physical-optics modelling of a millimetre-wave imaging system intended to enable automated detection of threats hidden under clothes. This paper outlines the theoretical basis of the formation of millimetre-wave images and provides the model of the simulated imaging system. Results of simulated images are presented and the validation with real ones is carried out. Finally, we present a brief study of the potential materials to be classified in this system.
© 2006 Elsevier B.V. All rights reserved.

Keywords: Millimetre-wave; Image formation; Image simulation; Kolmogorov–Smirnov test; Material classification

1. Introduction

A recent increase in interest in millimetre-wave imaging has emerged from a requirement to protect public environments, such as airports, train stations and other public buildings. Of particular interest is the possibility of using a millimetre-wave imaging sensor for the automatic detection of suspect objects, such as weapons and explosives, hidden under clothes. The appearance of millimetre-wave images is very different from both conventional visible-light imagery and from closely related infrared imagery. This arises from the unusual physical regime where the wavelength of radiation is relatively long so that polarisation, angle-of-incidence effects, optical constants of scene components and partial coherence of the illumination impact significantly on the appearance of the scene. We describe here a modelling technique based on physical optics principles that enables the quantitative simulation of millimetre-wave imagery recorded using a new type of real-time personnel scanner.

We have three motivations for producing these synthetic images. Firstly, they provide a route to obtaining large numbers of video sequences for the training of detection, recognition and identification algorithms that would be otherwise expensive and problematic to record using real equipment. Second, synthesising images ensures that the imaging conditions are controlled and that the ground-truth is available (as the scene and its correspondence with the image is known). Lastly, image simulation enables pre-investigations on the influence of different physical parameters of the sensor, therefore enabling the exploration of both the phenomenology of the image formation and possible changes in the sensor set up.

Although there are many scene simulation tools available for visible light imaging and some for thermal imaging, these do not implement the physical regime of light interaction pertinent to millimetre-wave imaging. Surfaces are generally considered to be scattering (since the wavelength is short) and where specular reflections are implemented, these do incorporate the Fresnel coefficients for polarised light. Similarly both reflection and emission from specular surfaces at arbitrary angles is not incorporated. The issue of specularity is particularly important since the wavelength of millimetre-waves is long in comparison to surface irregularities of typical scene components in a personnel scanner so that all interactions are predominantly specular and polarisation sensitive. Similarly millimetre-wave imagers generally employ polarised illumination and detection. Although the spatial coherence of the source is reduced

* Corresponding author. Tel.: +44 131 451 3299; fax: +44 131 451 4155.
E-mail address: bg5@hw.ac.uk (B. Grafulla-González).

0167-8655/$ - see front matter © 2006 Elsevier B.V. All rights reserved.
doi:10.1016/j.patrec.2006.02.002

by the illumination system, the remaining degree of coherence is sufficient to introduce significant speckle; this is also not incorporated into conventional simulation tools.

The simulation tool described here incorporates all of the above effects to yield a quantitative radiometric calculation of fluxes at each detector pixel. A wide literature exists on the radiometric analysis of the millimetre-wave image formation. Some useful references about this subject are Grafulla-González et al. (2005), Sinclair et al. (2000, 2001), Yujiri et al. (2003), Wilson et al. (1986), Haworth et al. (2004) and Anderton et al. (2001). To the best of our knowledge, very little work has been reported on the simulation of millimetre-wave images for personnel scanners, although some of the above issues were addressed by Salmon (2004a,b) and Salmon et al. (2002).

Consequently, the main contributions of our work lie in two different aspects. The first one is the description of a full model of millimetre-wave image formation, including the residual coherent illumination and the speckle noise in the synthetic images. In addition we describe a comparison between real and synthetic images, validating therefore our model.

To implement the simulator we adopted a hybrid solution, combining commercial optical ray-tracing software *Zemax* to trace rays within the scene and *Matlab* to implement physical optics aspects of the image formation using the ray data provided by *Zemax*. This solution enables the definition of the geometry of the scene as well as the implementation of the Fresnel coefficients for specular reflections from the physical parameters of the materials. Full non-sequential ray tracing and multiple reflections are implemented. Its novelty lies in the fact that it models the physical processes at millimetre-wavelength, whilst allowing full definition of the scene, the materials and the illumination. To some degree, this is a pragmatic solution: the use of ray tracing partially neglects diffraction effects and this will introduce some inaccuracies. A rigorous implementation employing rigorous electromagnetic theory may yield greater accuracy, but the computation power required for a scene of such complexity would be excessive.

This paper is divided into three parts. The description of the full model of millimetre-wave image formation is presented in Section 2, where the radiometric analysis and the noise modelling is explained. In Section 3, the simulation of these images is described. We will explain how it has been carried out as well as the basis for the material discrimination. Finally, in Section 4 we will present the validation of the synthetic images using the Kolmogorov–Smirnov test and the results obtained with the simulator.

2. Formation of millimetre-wave images

Two dominant phenomena in the formation of millimetre-wave images are (1) the combination of emitted and reflected radiation from scene components (radiometry analysis) and (2) the modification of the ideal image of the scene by the instrumental response; this includes the imager impulse response and noise artifacts.

2.1. Radiometry analysis

For the modelling conducted here, the radiation frequency is $f = 35$ GHz or equivalently $\lambda \approx 9$ mm in wavelength. This frequency is a compromise between the competing influences of higher frequency for improved resolution and lower frequency for reduced cost. The focal length of the imager is 0.8 m resulting in a diffraction-limited spot-size at the object of $\sim$2 cm. We consider only short-range indoor scene (the influence of the atmosphere is neglected) with mostly incoherent illumination (Coward and Appleby, 2003). It is important to note that the illumination source has some residual spatial and temporal coherence and this is evident as low-level speckle noise is present in the images.

The temperature of the objects in the scene is above absolute zero and so scene components radiate power with an efficiency determined by the emissivity ϵ. Since the surfaces of the body and threats are flat on the scale of the wavelength, the reflections are considered specular (Sinclair et al., 2000). This implies that scattering effects are small and propagation of light within the scene will satisfy to ray optics approximations. This approximation will break down to some extent for smaller scale structures, such as fingers, facial features, etc. The intensity of millimetre-wave radiation at each pixel is determined by contributions from both self-emission by scene components and reflections from illumination sources both within and external to the scene. Illumination of the scene is by ambient, background black body radiation with a temperature in the region of 290 K and by extended and diffuse active sources with elevated equivalent temperatures of, typically, 800 K. The reflectivity, R, the emissivity, ϵ, and the transmissivity t for optically thick components are related by Salmon et al. (2002):

$$R + \epsilon + t = 1 \tag{1}$$

These three coefficients depend on the physical characteristics of the materials and other geometrical aspects of the scene defined via the dielectric constant ε, the permeability μ, the angle of incidence θ_i, the angle formed between the electric field and the plane of incidence α, and the polarisation p. Note that any of these coefficients can be expressed as a sum of the projections of the coefficient in orthogonal and parallel polarisation planes; the power reflectivity is then given by Born and Wolf (1987):

$$R(\varepsilon, \mu, \theta, \alpha) = R_p(\varepsilon, \mu, \theta)\cos^2\alpha + R_s(\varepsilon, \mu, \theta)\sin^2\alpha \tag{2}$$

where the subscripts p and s denote p- and s-polarisation. Similar equations can be obtained for transmissivity and emissivity:

$$t(\varepsilon, \mu, \theta, \alpha) = t_p(\varepsilon, \mu, \theta)\cos^2\alpha + t_s(\varepsilon, \mu, \theta)\sin^2\alpha \tag{3}$$

$$\epsilon(\varepsilon, \mu, \theta, \alpha) = \epsilon_p(\varepsilon, \mu, \theta)\cos^2\alpha + \epsilon_s(\varepsilon, \mu, \theta)\sin^2\alpha \tag{4}$$

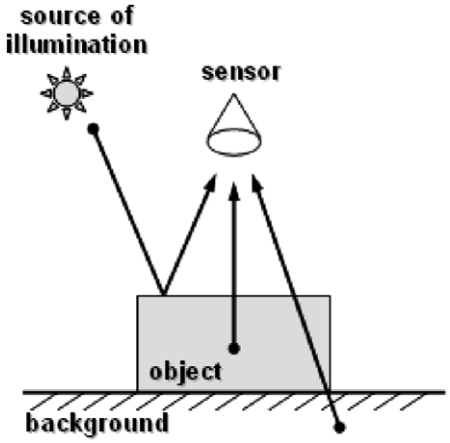

Fig. 1. One of the different phenomena influencing the formation of millimetre-wave images: the combination of power from various components present in the scene.

Since the active source is mostly incoherent, the three different intensity coefficients in Eq. (1) are summed (Fig. 1), yielding

$$T_{\text{rec}}(\varepsilon,\mu,\theta,\alpha) = RT_{\text{ill}} + \epsilon T_{\text{obj}} + tT_{\text{back}} \tag{5}$$

which describes the received temperature at the input of the sensor (Sinclair et al., 2001): where $T_{\text{rec}}(\varepsilon,\mu,\theta,\alpha)$ is the received temperature, T_{ill} the temperature of the illumination, T_{obj} the temperature of the object and T_{back} the temperature of the background. T_{ill}, T_{obj} and T_{back} are constant values.

2.2. Sensor effects

Sensor effects are modelled according to the schematic shown in Fig. 2. This describes the weighting given to the scene thermal emission (which is spatially incoherent and hence is modified by the imager PSF) and two reflected components due to partially coherent illumination by an extended source. This partial coherence is considered as a weighted sum of an incoherent component (modified by the imager PSF) and a coherent component (modified by the imager impulse response). It is this latter component that gives rise to multiplicative speckle in the image.

Incoherent scene components are transformed by the convolution with the point spread point function (PSF) of the imager. As the aperture is circular, the PSF is modelled as an Airy disk (Goodman, 1996):

$$\text{PSF} = |h(q)|^2 = I_0\left[\frac{2J_1\left(\frac{kaq}{R}\right)}{\frac{kaq}{R}}\right]^2 \tag{6}$$

where $h(q)$ is the impulse response of the system, $J_1(\cdot)$ is the Bessel function of first kind, $k = \omega\sqrt{\mu\epsilon}$ the wave number, a the radius of the aperture, $q = \sqrt{x^2+y^2}$ the coordinates of the point in the image plane, R the range between the aperture and the object, and I_0 the irradiance at the center of the pattern. Out-of-focus components are convolved with an approximation to an out-of-focus PSF and so appear blurred in the simulated images. The resulting image $I_{\text{psf emi}}$ is presented in Fig. 3(a).

The component due to reflection of the source is due to the weighted sum of an incoherent component, that is convolved with the imager PSF and a coherent part that is convolved with the imager impulse response. The w_1 and w_2 in the weighted sum are related as

$$w_1 + w_2 = 1 \tag{7}$$

The resulting image $I_{\text{psf ref}}$ is presented in Fig. 3(b).

For the coherent component of the illumination, the amplitude and phase image resulting from the radiometry analysis, I_{amp}, is convolved with the impulse response of the system. This amplitude image is generated using:

$$I_{\text{amp}} = \sqrt{I_{\text{int}}}e^{j\psi} \tag{8}$$

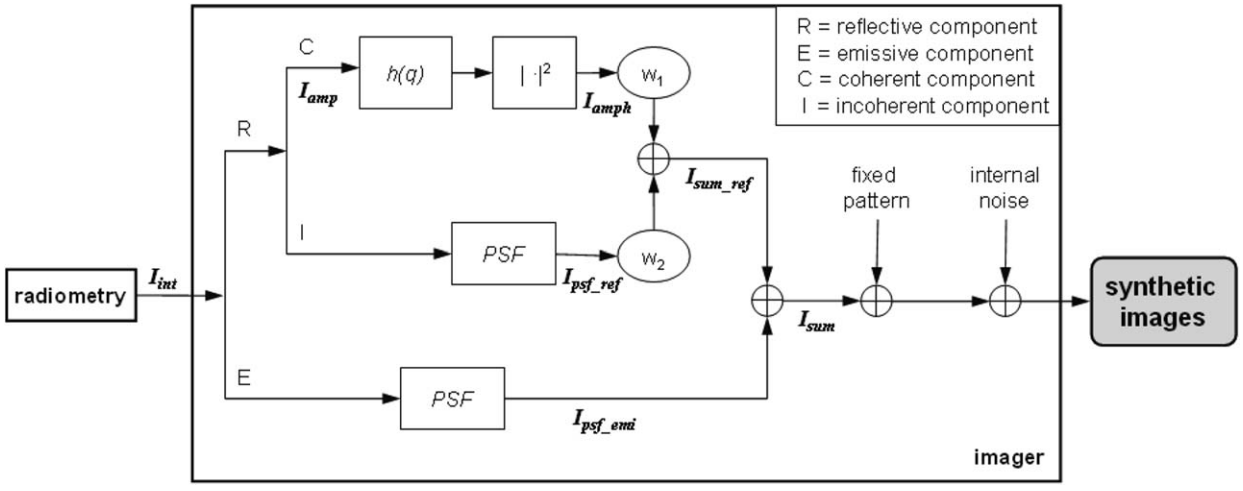

Fig. 2. The sensor effects are modelled by the effects of the imager and the combined effects of noise generated by the electronic devices and random variations in the received signal. The result of the system yields the synthetic millimetre-wave image.

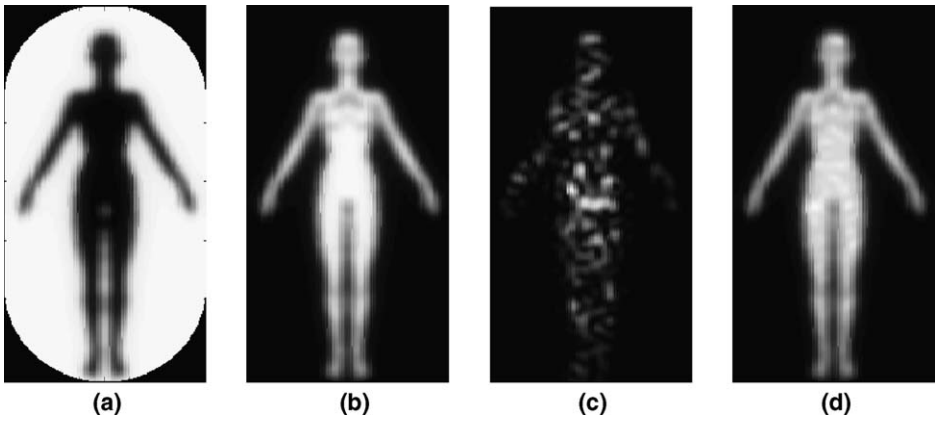

Fig. 3. Intermediate images of the noise model: (a) convolved background $I_{\text{psf emi}}$, (b) incoherent image $I_{\text{psf ref}}$, (c) coherent image I_{amph} and (d) weighted sum $I_{\text{sum ref}}$.

where ψ is the phase of the radiation at the detector received from the image including the phase of the illuminating signal. The method described here involves the calculations of all path lengths and so, provided the phase characteristics of the source can be calculated, the phase can be incorporated. In practice, it is very difficult to obtain reliable information on the illumination phase and so as a practical solution, we have assumed the combination of illumination phase and geometrical propagation distances to result in a random variable phase with a Gaussian distribution. The standard deviation of this distribution should be greater than about 2. The impulse response is given by the Airy distribution (Goodman, 1996):

$$h(q) = \frac{\sqrt{I_0}}{j}\left[\frac{2J_1\left(\frac{kaq}{R}\right)}{\frac{kaq}{R}}\right] \tag{9}$$

The resulting amplitude image I_{amph} and the weighted sum image $I_{\text{sum psf}}$ are presented in Fig. 3(c) and (d), respectively.

Finally, the internal noise contributed by the receiver electronics and the imager itself is added (Fig. 2). These noises are modelled as a gaussian distribution whose mean and standard deviation are estimated from a set of real data (see Section 4). The resulting image yields the synthetic millimetre-wave image.

3. Simulation of millimetre-wave images

In the synthetic images, the scene is generally composed of a body and one or several threats (weapons, knives, explosives, etc.). The body is incorporated as a triangle faceted CAD model (Fig. 4(a)) and threats as metallic or dielectric patches over the body. The typical scene is described in Fig. 4(b) and the dimension used shown in Table 1.

Each object is modelled according to its physical characteristics: the dielectric constant ε_{obj}, the permeability μ_{obj}

Table 1
Dimensions of the scene

Description	Length (m)
Range object—closest part of the imager	1.6
Range object—aperture	2.9
Focal length	0.8
Lens diameter	1.6
Height of the body	1.8
Dimensions of the threat	0.075×0.075

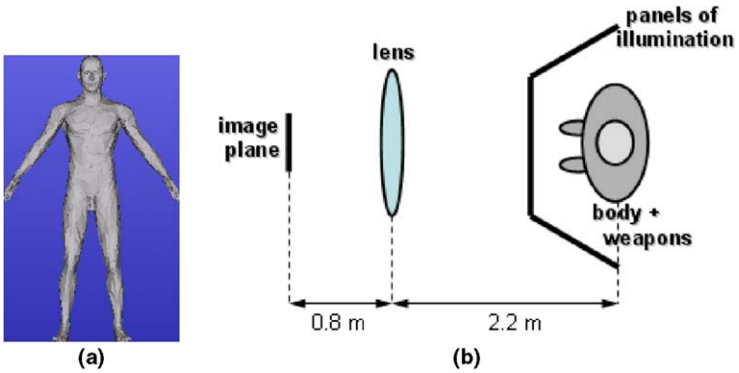

Fig. 4. The scene is composed of a body, a lens and an image plane. (a) represents the CAD model (stl file) used to model the body, and (b) the position of the various objects in the scene. Note that the rays are defined to pass through the centre of the lens.

Table 2
Physical object characteristics

Body	$\varepsilon_{body} \approx 28 - i34$	$T_{body} \approx 310$
Metal	$\varepsilon_{metal} \approx 1 - i510^6$	$T_{metal} \approx 308$
Plastic	$\varepsilon_{plastic} \approx 2.2$	$T_{plastic} \approx 308$

(which is unity for non-magnetic materials considered here) and the physical temperature T_{obj}. The value of the dielectric constant depends on the type of material. Therefore, the image grey level actually reflects an intrinsic property of the materials. This means that millimetre-wave images can be used for material classification. In the simulator, flesh, one of the most relevant materials, is modelled as salty water (Ulaby et al., 1986) and therefore its dielectric constant will be $\varepsilon_{body} \approx 28 - i34$. Examples of the physical characteristics of other pertinent materials are presented in Table 2.

Fig. 5 shows the reflectivity as well as the received temperature for each material. As can be observed, metal is completely reflective and therefore the received temperature is equal to the illumination temperature irrespective of angle of incidence. For flesh, the reflectivity for angles of incidence less than about 60° is about 0.6. Furthermore, the transmissivity of flesh and can be neglected in implementing Eq. (1). This material, even if it is darker than the metal, is still detectable in a future classification. Finally, plastic has a very small reflectivity and emissivity. Consequently the transmissivity is high and the received temperature is almost equal to the received temperature of the material imaged through it. This property makes the plastic a very difficult material to classify.

Two software tools have been used to carry out the simulation of millimetre-wave images. A ray-tracing programme, *Zemax*, is used to propagate rays back from each detector pixel via reflections from scene components to the source: either the illumination source or the background. All reflected and multiply reflected rays within the scene are characterised using the non-sequential ray-tracing mode of *Zemax* and the information about every ray history is stored as a text file. By repeated application of Eq. (5) at each intercept of a ray with a scene component it is possible to calculate the intensity of millimetre-wave radiation incident occurring at each detector scene pixel. This component of the simulation is executed by reading the *Zemax* output text file with *Matlab* which is used to calculate the equivalent temperatures at each pixel. Convolution of these images with the imager point spread function and the addition of stochastic low level speckle noise to images yields the simulated millimetre-wave image.

The ray-optics model used here is strictly valid only when the scene dimensions are large compared to a wavelength, that is, larger than a few centimetres. If this condition is not satisfied then accurate modelling requires the rigorous electromagnetic methods that are appropriate for unbounded problems, such as the boundary element method. In the imaging of a person with millimetre-waves the ray-optics method will provide accurate results for the larger body parts with large radii of curvature, but some inaccuracies might be expected for smaller features such as the fingers and details of the face. These inaccuracies may become noticeable with future improvements in detector technology, but currently noise levels and departures between the parameters of the modelled system and the actual system are too large for them to be observed. The salient advantage of employing a ray optics model is in the speed of computation and implementation and this is vital for the simulation of large numbers of video sequences that are required for training automated detection algorithms.

4. Results of millimetre-wave images

Fig. 6 presents simulated millimetre-wave images for different values of the weight w_1 of the coherent proportion of the illumination and the standard deviation σ of the internal noise. The observed "similarity" between the real and synthetic images is very subjective, and therefore a quantitative validation is required to compare real and synthetic images.

There are two different aspects to be validated in the simulator: (1) the noises (i.e., the sensor effects) and (2) the physical model (i.e., the radiometric analysis). In order to carry out quantitative validations, the following steps are done.

- Normalisation of the real and synthetic data in order to match both the mean of the background and the mean of the object.

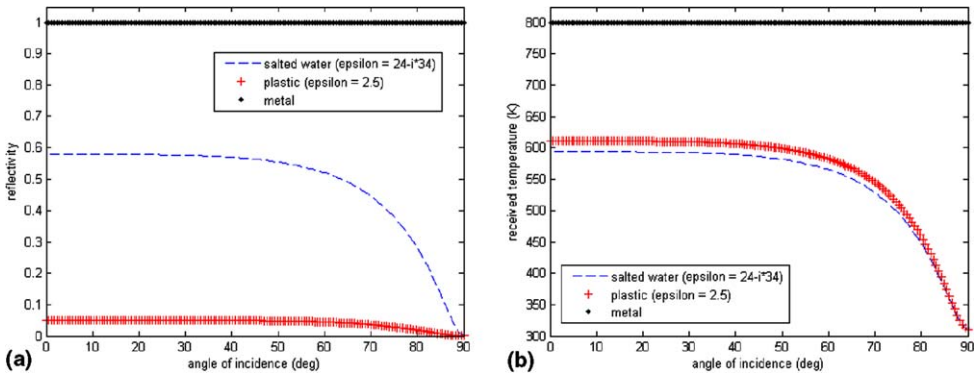

Fig. 5. Reflectivity (a) and received temperature (b) for different materials.

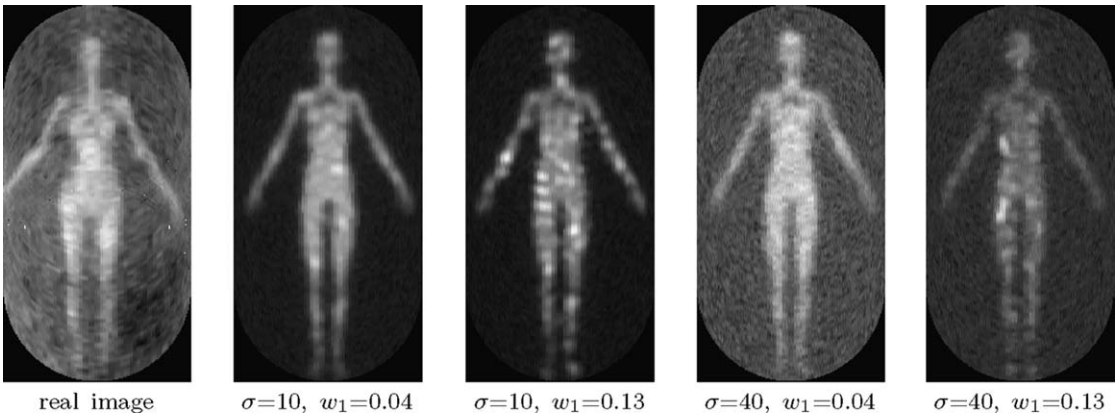

Fig. 6. Some examples of millimetre-wave images.

- Estimation of the values of σ and w_1 that minimize the D-statistic, i.e., the value $D_{m,n}$ (Appendix A), for both the object and background distributions.
- Use of the Kolmogorov–Smirnov test (Appendix A) to evaluate the validity of the noise models in both the background and object areas.
- Comparison of the cross-sections, on similar scenes, of both the real and synthetic images to validate the physical model.

For the noise validation, we have carried out a non-parametric comparison between two data sets whose underlying cumulative distribution is unknown. The Kolmogorov–Smirnov test (Feller, 1948; Massey, 1950, 1951; Powers and Pao, 2005) establishes if these two data sets share the same distribution within some confidence intervals.

4.1. Parameter estimation

There are two parameters to estimate in our noise model: (1) the magnitude of the coherent component of the illumination, represented by the parameter w_1 and (2) the magnitude of noise that the imager introduces to the final image, represented by the standard deviation σ of the internal noise. These two parameters are estimated by comparing the real and synthetic data. However, a required preliminary step consists in first jointly normalizing both data sets to the same range of values (Fig. 7).

To carry out the normalisation, we have established that the relationship between real and synthetic data is a linear relation, described mathematically as follows:

$$T = aN + b \tag{10}$$

where T is the value of the synthetic data, N the value of the real data and (a, b) the gain and offset, respectively, of the normalisation process.

To calculate the values (a, b), we have considered the mean values of both the background and the object (Fig. 8), such that:

$$\begin{cases} \overline{T_{\text{back}}} = a\overline{N_{\text{back}}} + b \\ \overline{T_{\text{object}}} = a\overline{N_{\text{object}}} + b \end{cases} \tag{11}$$

where $\overline{T_{\text{back}}}$ and $\overline{N_{\text{back}}}$ are the mean values of the background area for simulated and real data respectively, and $\overline{T_{\text{object}}}$ and $\overline{N_{\text{object}}}$ the mean values of the object area for

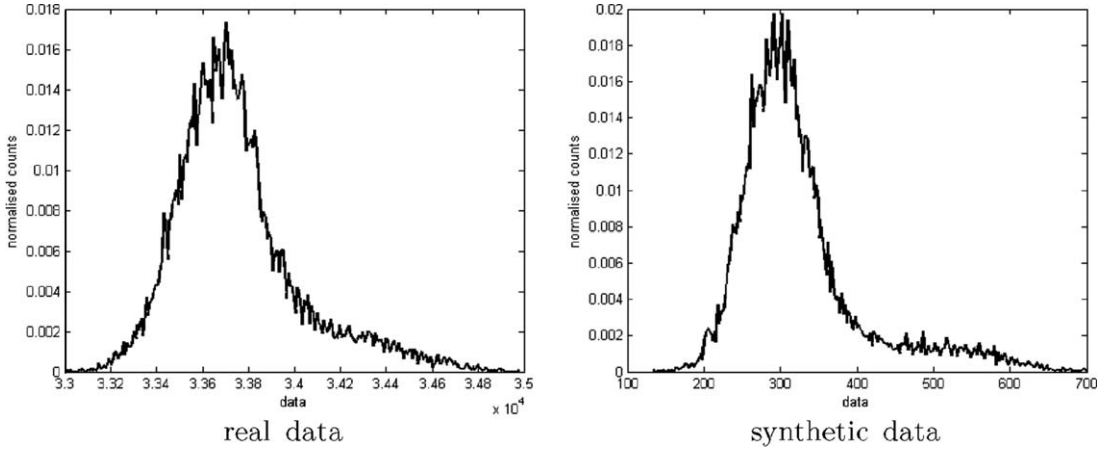

Fig. 7. Histograms for both the real and synthetic data.

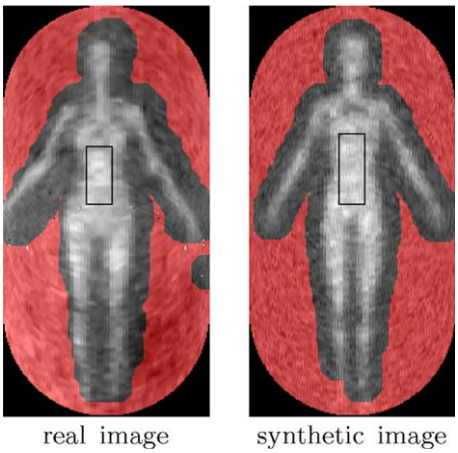

Fig. 8. Normalisation areas: background in brighter area and object delimited in black.

simulated and real data, respectively. The result of the normalisation process is then presented in Fig. 9.

We next estimate the noise parameters that yield a best fit between the real and simulated images. Using these parameters, we will then validate the noise models using the Kolmogorov–Smirnov test to compare the respective distributions of the real and the synthetic noise.

The background is not affected by coherent light effects, only the internal noise effects will be present. The parameter σ is therefore estimated from the background. For values of w_1 spanning the typical values between 0 and 0.08, we calculate the value of $D_{m,n}$ between the real and synthetic data of the background, for σ varying between 10 and 55. Fig. 10(a) shows the resulting curves, from where the value of σ is estimated: $\sigma \sim 40$.

Once the value of σ is set, the value of w_1 is estimated similarly. In this case, the value of $D_{m,n}$ is calculated for the object area. Fig. 10(b) shows the resulting curve, where the minimum $D_{m,n}$ is at $w_1 = 0.04$.

Finally, as the values of σ and w_1 are estimated, we can generate the simulated image, presented in Fig. 11. Note that elliptical artifacts due to the scanning process (Coward et al., 2004) are present in both real and synthetic images.

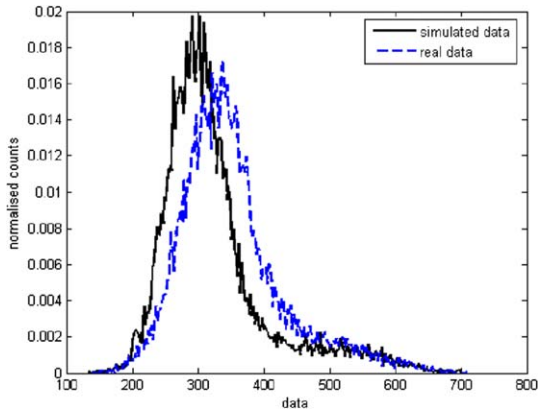

Fig. 9. Real and synthetic histograms after normalisation process.

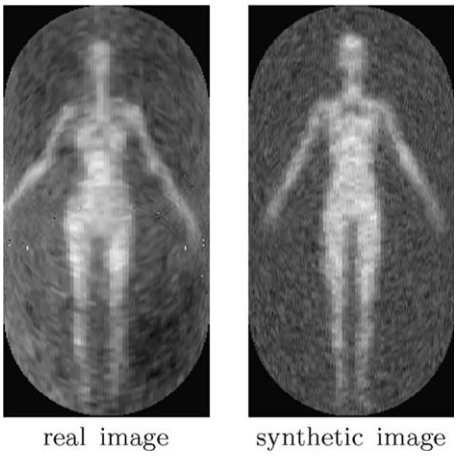

Fig. 11. Real image and synthetic image generated with the estimated parameters.

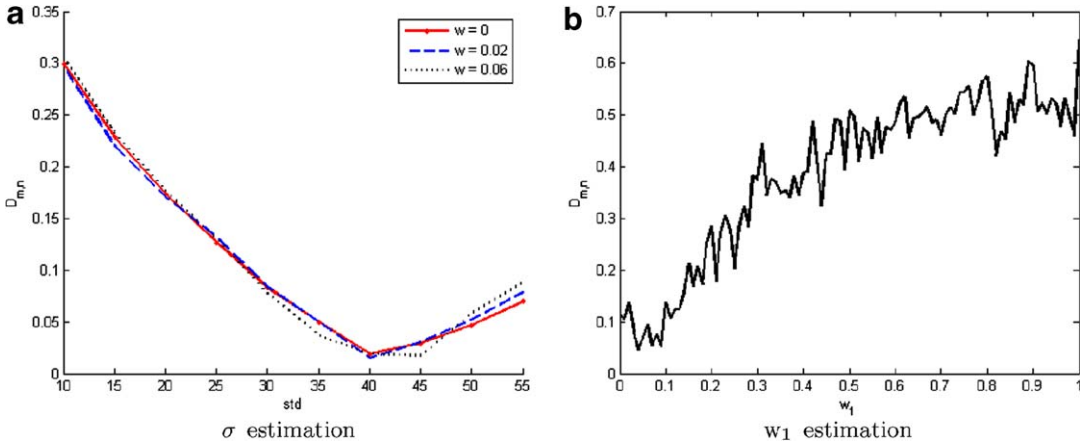

Fig. 10. Parameter estimation: (a) $\sigma = 40$ and (b) $w_1 = 0.04$.

4.2. Noise validation

To validate the noise levels in both the background and the object area, the non-parametric Kolmogorov–Smirnov test is used. The procedure of this test is as follows:

- Calculation of the value of $D_{m,n}$ for the two data sets to be compared.
- Comparison of this value to a threshold $d_\alpha(N)$, which only depends on the number of samples of the two data sets.
- If $D_{m,n} \leqslant d_\alpha(N)$, then the hypothesis $H_0: S_n(x) = T_m(y)$ is verified, and therefore the two data sets can be considered to have the same distribution within the confidence interval.
- On the opposite, if $D_{m,n} \geqslant d_\alpha(N)$, then the hypothesis $H_1: S_n(x) \neq T_m(y)$ is verified, and therefore the distributions of the two data sets are different.

In our case, the values of this test are presented in Table 3. In both the background and the body areas, the Kolmogorov–Smirnov test is positive, and hence the distributions of the real and synthetic data are considered to be the same. Consequently, the noise model for both areas is validated. Finally, Fig. 12 shows the comparison between cumulative distribution functions and histograms of the real and synthetic data. It can be noticed that effectively real and synthetic data have very similar distributions.

Table 3
Results of the Kolmogorov–Smirnov test

	m	n	N	Threshold	$D_{m,n}$	H_0
Background	4857	8042	30281	0.0247	0.0121	Verified
Object	169	240	99	0.1364	0.1099	Verified

4.3. Physical model validation

To validate of the physical model, we compare different cross-sections in the real and simulated image, and estimate the root mean square error (RMSE) between them:

$$\mathrm{RMSE} = \sqrt{\frac{1}{M}\sum_{i=1}^{M}[I_{\mathrm{real}}(i) - I_{\mathrm{sim}}(i)]^2} \tag{12}$$

where $I_{\mathrm{real}}(i)$ is the ith sample of the cross-section of the real image, $I_{\mathrm{sim}}(i)$ the ith sample of the cross-section of the simulated image and M the total number of points in the cross-section.

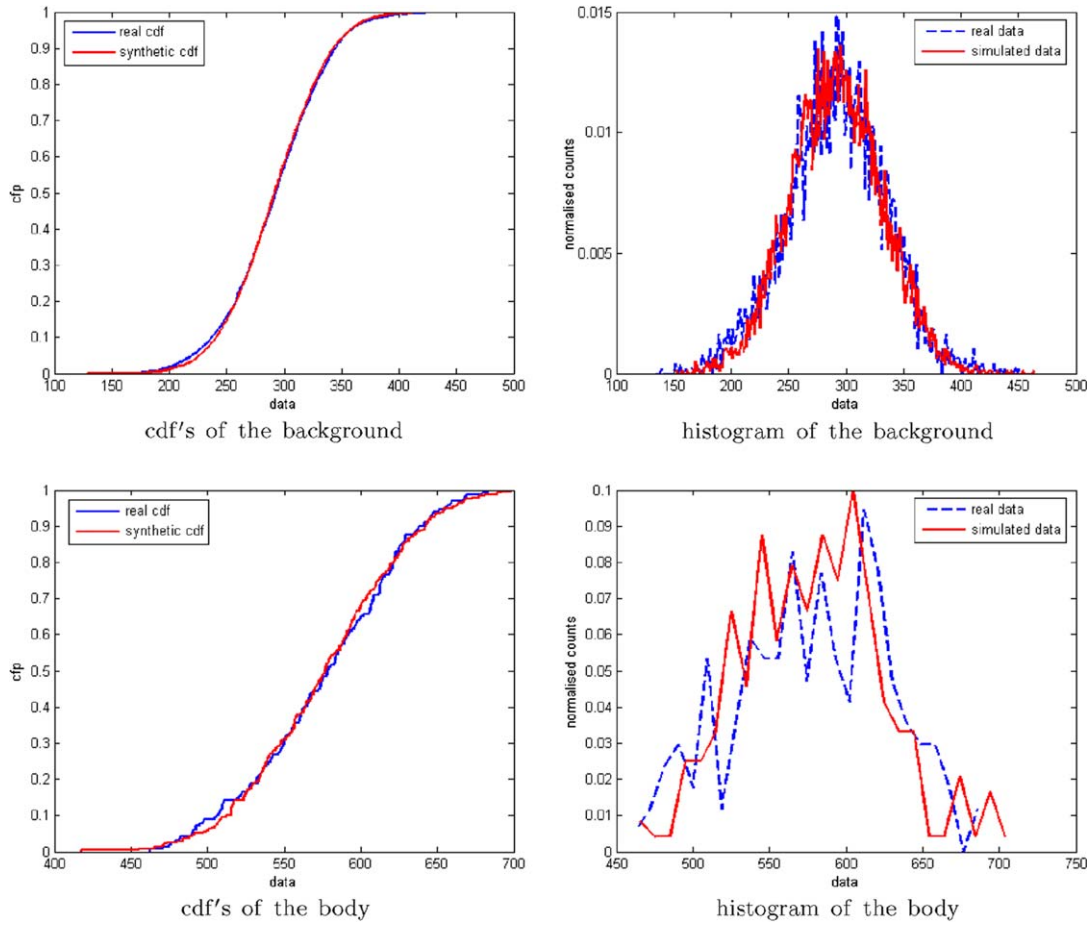

Fig. 12. Comparison of the empirical cumulative distribution function and histograms between real and synthetic data for the background and body.

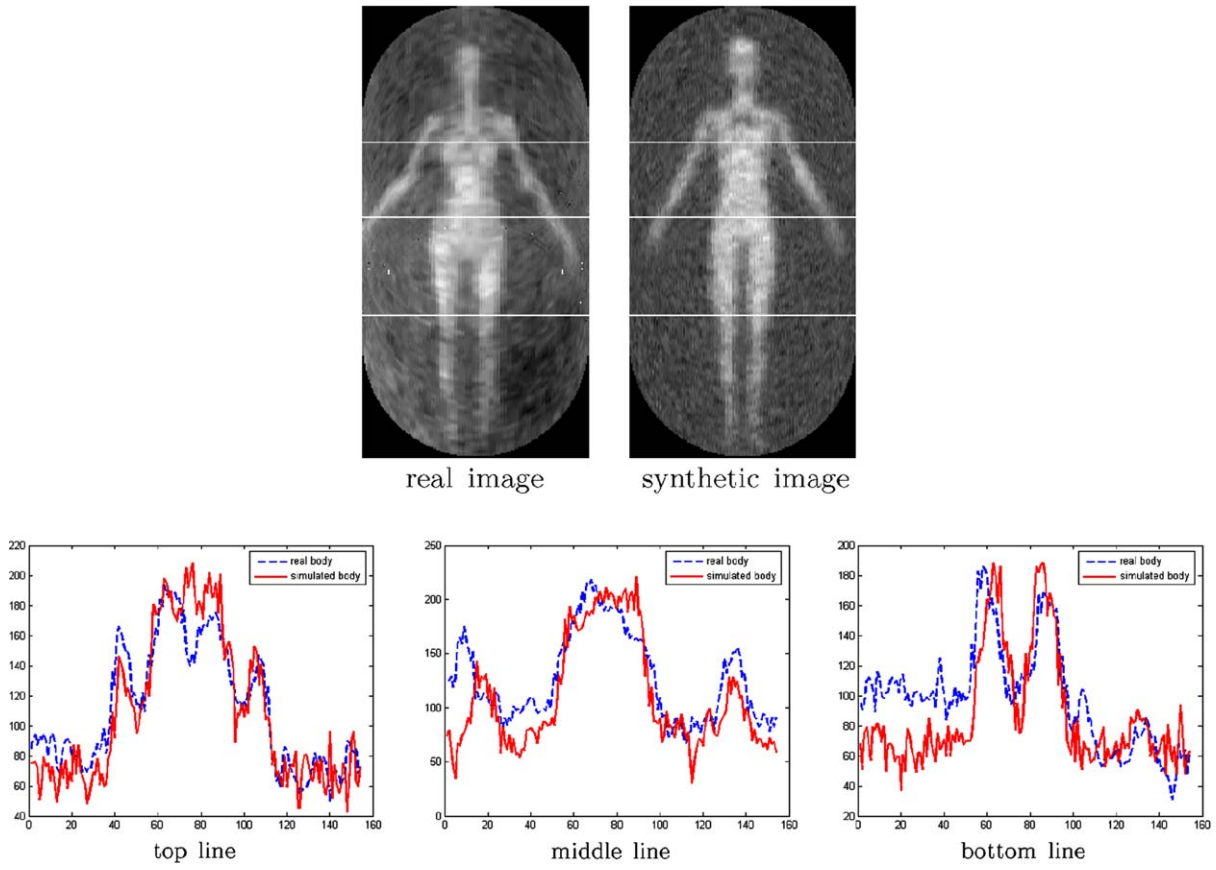

Fig. 13. Comparison between the real and simulated cross-sections of the body.

Table 4
Results of the RMSE

	Top line	Middle line	Bottom line
Absolute RMSE	10.0110	12.4212	11.3845
Relative RMSE	3.91%	4.85%	4.45%

Fig. 13 shows the comparison for different cross-sections, and Table 4 presents the values of the absolute and relative RMSE for each cross-section.

Current plots show that the dynamic of the simulated cross-sections are very similar to the real ones, reinforced by the fact that the values of the RMSE for all the cases are small compared to the typical values of the images: around 4% of error. The strongest discrepancies, to the right of the middle and bottom lines, are due to respectively a difference in the position of the arm of the CAD model and the real person, and low frequency spacial artefacts in the background (the lower left part of the background is brighter), which the simulator does not model.

5. Conclusion and future work

In this paper, we have described the physics underpinning millimetre-wave scene simulation and presented a physical optics simulation of millimetre-wave images using commercial optical ray-tracing software and *Matlab*. Our initial results show that it is possible to recreate real scenarios by means of their physical and geometrical characteristics. Synthetic images are obtained with reliable quality compared to real images according to the validation carried out.

Future work aims at three different aspects. Further physical model validation is needed, especially regarding new materials and fully controlled scenes. In this way, shapes easily modelled should be used (as for example, panels or cylinders). As outlined, the millimetre-wave images reflect the physical properties of material and therefore potentially enable material classification. The simulator will enable the exploration of modifications of the sensor so as to enhance its material discrimination capability. One possibility is to fuse image information from different sensor configurations (lighting, polarisation, frequency).

Acknowledgements

The author would like to acknowledge the support of QinetiQ. Beatriz Grafulla-González is supported by EPSRC Research Grant GRS/68088 "ATRIUM" under the Think Crime programme.

Appendix A. The Kolmogorov–Smirnov test

Let $(x_1, x_2, \ldots, x_n)$ and $(y_1, y_2, \ldots, y_m)$ be two data sets of size n and m, respectively, n and m not necessarily equal, of mutually independent random variables having a common continuous cumulative distribution $F(x)$, and $(x_1^*, x_2^*, \ldots, x_n^*)$ and $(y_1^*, y_2^*, \ldots, y_m^*)$ the rearranged data sets in increasing order of magnitude. Let $S_n(x)$ and $T_m(y)$ be the corresponding empirical cumulative distribution functions defined by

$$S_n(x) = \begin{cases} 0 & \text{for } x < x_1^* \\ \dfrac{k}{n} & \text{for } x_k^* \leqslant x < x_{k+1}^* \\ 1 & \text{for } x \geqslant x_n^* \end{cases} \qquad T_m(y) = \begin{cases} 0 & \text{for } y < y_1^* \\ \dfrac{k}{m} & \text{for } y_k^* \leqslant y < y_{k+1}^* \\ 1 & \text{for } y \geqslant y_m^* \end{cases} \tag{A.1}$$

The hypothesis we would like to verify within given confidence intervals $d_\alpha(N)$ (i.e., the null hypothesis) is defined such that:

$$H_0 : S_n(x) = T_m(y) \tag{A.2}$$

We define a new random variable $D_{m,n}$, which only depends on the number of samples in each data set:

$$D_{m,n} = \sup |S_n(x) - T_m(y)| \tag{A.3}$$

The distribution of $D_{m,n}$ is not known, however (Feller, 1948) it can be demonstrated that the random variable $N^{\frac{1}{2}}D_{m,n}$ (where $N = \frac{mn}{m+n}$) tends towards a limiting cumulative distribution, $L(z)$, as $m \to \infty$, $n \to \infty$, and $\frac{m}{n} \to a$, where a is a constant. The limiting cumulative distribution $L(z)$ is expressed as

$$L(z) = 1 - 2\sum_{j=1}^{\infty}(-1)^{j-1}\mathrm{e}^{-j^2z^2} \tag{A.4}$$

Summarising:

$$\lim_{m,n\to\infty} Pr\left\{N^{\frac{1}{2}}D_{m,n} \leqslant z\right\} = L(z) \tag{A.5}$$

and rearranging terms we obtain:

$$\lim_{m,n\to\infty} Pr\left\{D_{m,n} \leqslant N^{-\frac{1}{2}}z\right\} = L(z) \tag{A.6}$$

The null hypothesis is verified if the values are under a certain threshold $d_\alpha(N) = N^{-\frac{1}{2}}z$ (which is equivalent to write that both cumulative distribution functions are within the same confidence interval $d_\alpha(N)$). On the other hand, the probability of rejection can be written as

$$\lim_{m,n\to\infty} Pr\{D_{m,n} \geqslant d_\alpha(N)\} = 1 - Pr\left\{D_{m,n} \leqslant N^{-\frac{1}{2}}z\right\} = \alpha \tag{A.7}$$

and verifies the so-called alternative hypothesis, that is:

$$H_1 : S_n(x) \neq T_m(y) \tag{A.8}$$

We set arbitrarily that the probability of acceptance of the null hypothesis is 0.95 (or probability of rejection = 0.05), i.e., $L(z) = 0.95$, which gives a value of z of 1.3581 (Smirnov, 1948). And finally, the threshold for the null hypothesis is calculated as

$$d_\alpha(N) = \frac{1.3581}{\sqrt{N}} \tag{A.9}$$

References

Anderton, R.N., Appleby, R., Coward, P.R., Kent, P.J., Price, S., Sinclair, G.N., 2001. Security scanning at 35 GHz. In: Smith, R.M., Appleby, R. (Eds.), SPIE Proceedings, Passive Millimeter-Wave Imaging Technology V, vol. 4373. pp. 16–23.

Born, M., Wolf, E., 1987. Principles of Optics, sixth ed. Pergamon Press.

Coward, P., Appleby, R., 2003. Development of an illumination chamber for indoor millimetre-wave imaging. In: Appleby, R., Wikner, D.A., Trebits, R., Kurtz, J.L. (Eds.), SPIE Proceedings, Passive Millimeter-Wave Imaging Technology VI and Radar Sensor Technology VII, vol. 5077. pp. 54–61.

Coward, P.R., Anderton, R.N., Price, S., October 2004. Receiver array design for conically scanned millimetre-wave imagers. In: Appleby, R., Chamberlain, J.M., Krapels, K.A. (Eds.), SPIE Proceedings, Passive Millimetre-Wave and Terahertz Imaging and Technology, vol. 5619. pp. 108–116.

Feller, W., 1948. On the Kolmogorov–Smirnov limit theorems for empirical distributions. The Annals of Mathematical Statistics 19 (2), 177–189.

Goodman, J.W., 1996. Introduction to Fourier Optics. McGraw-Hill International Editions.

Grafulla-González, B., Tomsin, M., Lebart, K., Harvey, A.R., 2005. Modelling of millimetre-wave personnel scanners for automated detection. In: Proceedings of the IEE International Symposium on Imaging and Crime Prevention. pp. 9–13.

Haworth, C.D., Grafulla-González, B., Tomsin, M., Appleby, R., Coward, P., Harvey, A.R., lebart, K., Petillot, Y., Trucco, E., 2004. Image analysis for object detection in millimetre-wave images. In: Appleby, R., Chamberlain, J.M., Krapels, K.A. (Eds.), Passive Millimetre-Wave and Terahertz Imaging and Technology, vol. 5619. pp. 117–128.

Massey, F.J.J., 1950. A note on the estimation of a distribution function by confidence limits. The Annals of Mathematical Statistics 21 (1), 116–119.

Massey, F.J.J., 1951. The Kolmogorov–Smirnov test for goodness of fit. Journal of the American Statistical Association 46, 68–78.

Powers, R.M., Pao, L.Y., December 2005. Using Kolmogorov–Smirnov tests to detect track-loss in the absence of truth data. In: Proceedings of IEEE Conf. Decision and Control. pp. 3097–3104.

Salmon, N.A., August 2004a. Polarimetric scene simulation in millimetre wave radiometric imaging. In: Trebits, R., Kurtz, J.L., Appleby, R., Salmon, N.A., Wikner, D.A. (Eds.), Radar Sensor Technology VIII and Passive Millimeter-Wave Imaging Technology VII, vol. 5410. pp. 260–269.

Salmon, N.A., December 2004b. Scene simulation for passive and active millimetre and sub-millimetre wave imaging for security scanning and medical applications. In: Appleby, R., Chamberlain, J.M., Krapels, K.A. (Eds.), Passive Millimetre-Wave and Terahertz Imaging and Technology, vol. 5619. pp. 129–135.

Salmon, N.A., Appleby, R., Price, S., July 2002. Scene simulation of passive millimetre wave images of plastic and metal objects. In: Appleby, R., Holst, G., Wikner, D.A. (Eds.), SPIE Proceedings, Passive Millimetre Wave Imaging Technology VI, vol. 4719. pp. 397–401.

Sinclair, G.N., Appleby, R., Coward, P., Price, S., 2000. Passive millimetre wave imaging in security scanning. In: Smith, R.M., Appleby, R.

(Eds.), SPIE Proceedings, Passive Millimeter-Wave Imaging Technology IV, vol. 4032. pp. 40–45.

Sinclair, G.N., Anderton, R.N., Appleby, R., October 2001. Outdoor passive millimetre wave security screening. In: Proceedings of IEEE 35th International Carnahan Conference on Security Technology. pp. 172–179.

Smirnov, N., 1948. Table for estimating the goodness of fit of empirical distributions. The Annals of Mathematical Statistics 19 (2), 279–281.

Ulaby, F.T. et al., 1986. Microwave remote sensing, active and passive, vol. 3. Benjamin-Cummings.

Wilson, W.J., Howard, R.J., Ibbott, A.C., Parks, G.S., Ricketts, W.B., 1986. Millimetre-wave imaging sensor. IEEE Transactions on Microwave Theory and Techniques MTT-34 (10), 1026–1035.

Yujiri, L., Shoucri, M., Moffa, P., 2003. Passive millimeter-wave imaging. IEEE Microwave Magazine, 39–50.